Materials Research. 2024; 27:e20240081
DOI: https://doi.org/10.1590/1980-5373-MR-2024-0081

Influence of $FeCO_3$ and $FeSO_4$ Layers on Corrosion in Sulfuric Acid Medium of Eutetoid Steels

Francisco Felipe de M. Fideles[a], Mauro Andres C. Florez[a]*, Antonio Gomes de Souza Filho[b], Jorge Luiz Cardoso[a], Pedro Queiros Santiago[a], Walney Silva Araújo[a], Hamilton Ferreira G. de Abreu[a]

[a]Universidade Federal do Ceará, Departamento de Engenharia Metalúrgica e de Materiais, Programa de Pós-Graduação em Engenharia e Ciência de Materiais, Fortaleza, CE, Brasil.
[b]Universidade Federal do Ceará, Central Analitica, Departamento de Física, Fortaleza, CE, Brasil.

Received: February 18, 2024; Revised: May 08, 2024; Accepted: July 01, 2024

This work addresses the corrosion resistance of Riser steels used in submarine pipelines for oil production, making it crucial to evaluate the variables related to corrosion in the marine environment. Three types of wires with spheroidized, lamellar and discontinuous cementite microstructure were tested in 0.1M H_2SO_4 with and without the use of CO_2, in addition to a different ambient temperature (80 °C). Thus, electrochemical tests, including OCP and linear potentiodynamic polarization, revealed the corrosion resistance of each material. The analysis of the polarization curves through Tafel extrapolation, obtained the current density, correlating with the potential of the sample in the medium, indicating the polarization resistance. The LC wires demonstrated greater resistance to corrosion (769.23; 2,544.79 and 4,790.87 Ω.cm^2) compared to spheroidized cementite (502,40; 1,038.99 and 902.95 Ω.cm^2) and, which, in turn, obtained lower resistance values in two of the solutions. The $FeCO_3$ and $FeSO_4$ salts were formed in different areas, including the most degraded ones identified by Raman spectroscopy.

Keywords: *Tensile armatures, H_2SO_4, CO_2, Corrosion, Raman spectroscopy, $FeCO_3$, $FeSO_4$.*

1. Introduction

Steels for subsea applications are intended for application in aggressive and highly degraded environments—especially those with petroleum applications intended for producing and extracting offshore oil. Several structures are present in the oil fields, among which the production pipelines are exposed vertically, making the connection between the oil platform and the seabed, called risers, stand out[1]. These are divided into several layers that support the structure to resist the weather, as shown in Figure 1. However, some of these layers have already failed during their operation, which poses a risk to the installed structures[2].

The media in which risers are inserted is rich in NaCl, present in seawater, and other degrading compounds, especially those with sulfur[3,4], such as H_2SO_4, H_2SO_3, and H_2S. The objective of this work was to evaluate and compare the corrosion resistance of 3 wires used in the tensile reinforcement of risers using electrochemical tests of OCP and linear potentiodynamic polarization, observing the relationship of their microstructural morphologies with corrosion resistance, using H_2SO_4 and CO_2 as electrolyte. It was possible to evaluate oxides and salts formed on the surface of these materials, thus identifying the action of the medium in which it is inserted with the possible formation of protective layers, which can reduce corrosion in these materials[5,6].

*e-mail: mauro.cerra@ufc.br

2. Materials and Methods

The materials used were pearlitic eutectoid steels, used in tensile reinforcement in the form of wires, with different geometric profiles, as shown in Figure 2.

The chemical compositions of the wires are identified in Table 1. These data were obtained by means of the optical emission spectrometer.

2.1. Microstructural characterization of wires

Micrographs of the wires were obtained using the scanning electron microscope (SEM) Quanta 450 FEG – FEI. They were initially inserted in bakelite and sanded from 100 to 1200. They were then polished with 3 to 1 µm diamond paste. They were then washed with alcohol and dried. Nital 2% was used as a developing agent to develop their microstructures.

2.2. Electrochemical tests

The electrochemical tests were conducted in an electrochemical cell in an H_2SO_4 electrolyte medium with a concentration of 0.1 M, with and without the CO_2 atmosphere (99.99% purity), at a flow rate of 1 x10^{-4} m^3/s. Before the use of CO_2 the samples had been deaerated with N_2 and with the use of 80 °C and at room temperature. The samples used had a dimension of around 40 mm^2. They were embedded in epoxy resin, with a copper conductor wire attached to

Table 1. Chemical composition (%wt) of wires. Source: author.

wire	C	Mn	Si	S + P	Cr + Ni +V	Al	Mo +Ti	Fe
1	0.77	0.50	0.20	0.013	0.054	-	0.006	bal
2	0.76	0.56	0.18	0.015	0.040	-	0.005	bal
3	0.73	0.58	0.26	0.009	0.039	0.032	0.004	Bal

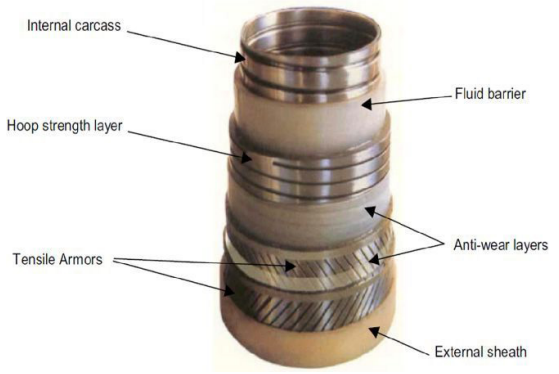

Figure 1. Identifying the Layers of a Flexible Riser[1]

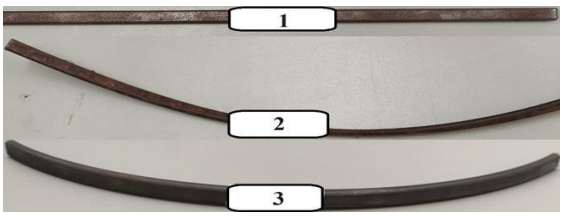

Figure 2. Wires in condition as received. 1 – straight (1.30 cm × 0.70 cm); 2 – twisted (1.20 cm × 0.60 cm) and 3 – curved (1.22 cm × 0.72 cm).

them so the electrical contact necessary for the tests could be performed. The samples were sanded with 100, 220, 320, 400, and 600 sanding sheets and then sprayed with alcohol and dried. The techniques of OCP (Open Circuit Potential) and LPP (Linear Potentiodynamic Polarization) were used in order to correlate this information with the Polarization Resistance (PR), which serves to identify the one that suffered the most corrosion damage under the indicated conditions. The reference electrode Ag/AgCl KCl (sat), platinum counter electrode, and the samples were used as working electrodes for these assays. The OCP time was set for 15 min when the samples were stabilized at their potential. Other relevant data used in the test were the cut-off current, which was 1 mA, and the curves were scanned from -0.1 V to 2.0 V of the OCP at a rate of 1 mV/s. Below is a summary of the operations performed with a table for preparing the tests — a different test condition for each wire, as shown in Table 2. From there, wires 1, 2, and 3 are termed spheroidized (SC), lamellar (LC), and discontinuous (DC) structured, respectively. These data were obtained according to information reported by an oil company that made the material available.

Table 2. Conditions for the execution of the experiments. Source: author.

Cementite condition	Condition in 0,1 M H_2SO_4
1 (SC), 2 (LC) and 3 (DC)	Saturated with CO_2 at 80 °C
1 (SC), 2 (LC) and 3 (DC)	Saturated with CO_2 at room temperature
1 (SC), 2 (LC) and 3 (DC)	Aerated and at room temperature

2.3. Raman spectroscopy

Raman spectroscopy was performed on the Witec Alpha 300 equipment with a gratin of 600 grooves/mm. The wavelength of the laser used to excite the material was 532 nm. The sample that obtained less severe corrosion resistance results was used for this technique. The peaks of Raman intensity evaluated were from 200 to 2000 cm^{-1}, included in references and databases, where oxides and salts are identified.

3. Results

3.1. Characterization of wires

The wires' microstructure was identified as pearlitic with varied cementite morphologies. Figure 3 shows the micrographs evaluated in this study. Figure 3a shows the wire with spheroidized cementite, classified this way by the presence of its globules. Figure 3b was classified as lamellar cementite due to lamellae alternating with the ferritic matrix. Finally, in Figure 3c, cementite has discontinuous characteristics with intermediate pro-files between balls and lamellar.

3.2. Eletrochemical tests

Graphs were obtained for OCP and linear potentiodynamic polarization due to the electrochemical tests. These are presented in Figures 4-9. These experiments used wires (spheroidized, lamellar, and discontinuous). The process was developed in 0.1 M H_2SO_4 medium mixed with and without CO_2 and at room temperature and 80 °C. During the tests, the pH was recorded using a pH meter, obtaining the following values for the respective solutions; saturated with CO_2 at 80 °C: pH 1–2; saturated with CO_2 at room temperature: pH 2–3; airy and at room temperature: pH 3–4.

3.2.1. Spheroidized cementite wire

Figures 4 and 5 below indicate OCP and linear potentiodynamic polarization for the spheroidized cementite wire, respectively.

Figure 5 shows the LPP data for the PCE wire.

Figure 4 shows the potentials of the spheroidized wire for each solution. The programmed time for OCP was 900 s (15 min), and the potential for this material in the evaluated

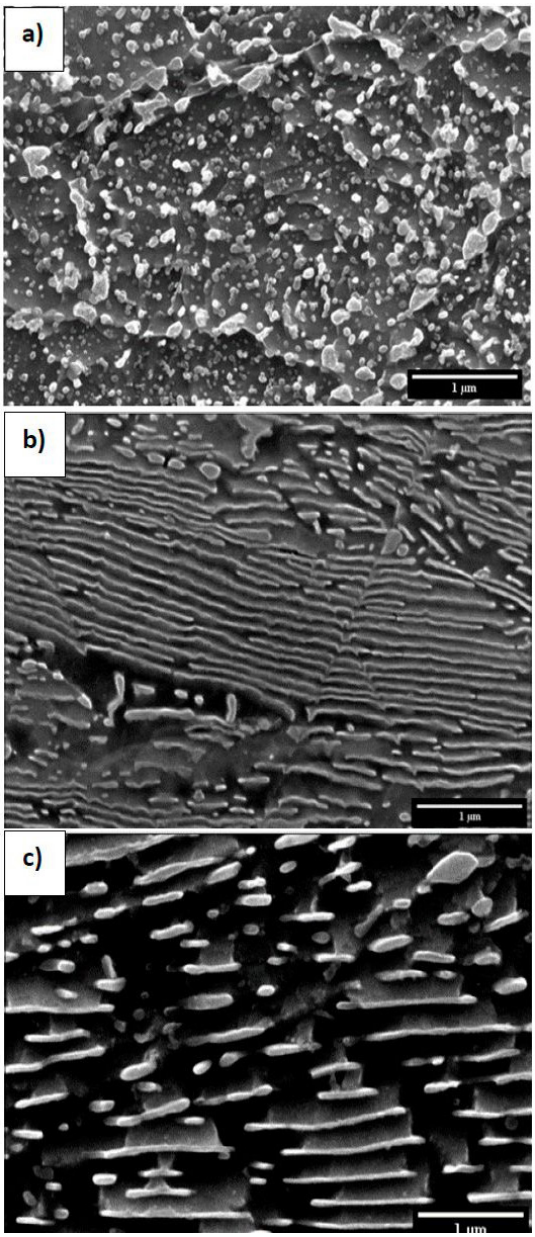

Figure 3. Microstructure of a) Spheroidized Cementite (SC), b) Lamellar Cementite (LC) and c) Discontinuous Cementite (DC).

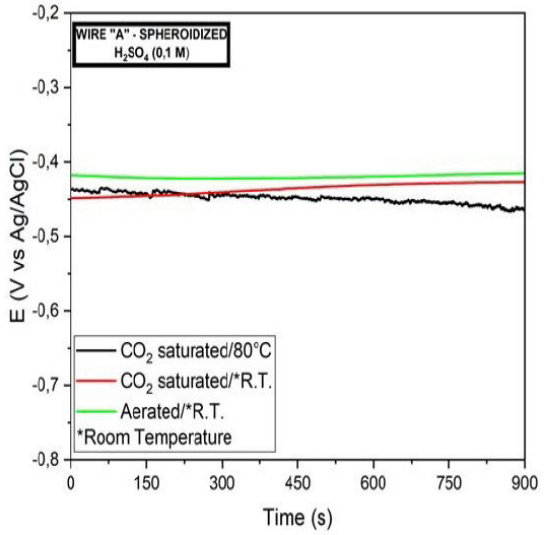

Figure 4. OCP curves for SC wire in the aqueous solution of 0,1M H_2SO_4 saturated with CO_2 at 80 °C, saturated CO_2 at room temperature (23 °C) and aerated at room temperature (23 °C).

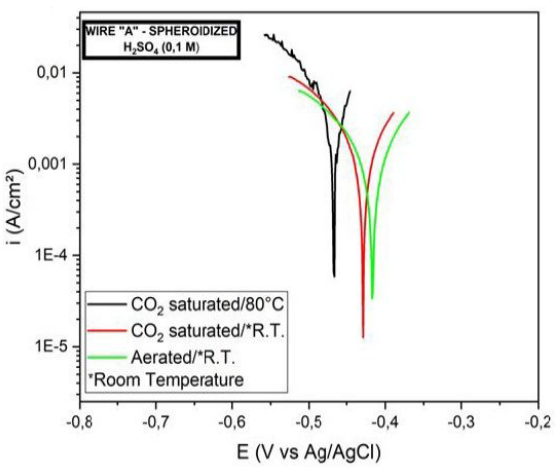

Figure 5. Potentiodynamic polarization curves for SC wire in the aqueous solution of 0,1 M H_2SO_4 saturated with CO_2 at 80 °C, saturated CO_2 at room temperature (23 °C) and aerated at room temperature (23 °C).

solutions was stabilized for other tests. The values obtained were between -0.4 and -0.5V.

In order to better show the corrosive power of these samples, in Figure 5, the linear potentiodynamic polarization graph was plotted, where it was possible to identify data about the current density. For spheroidized wire, the condition that obtained the lowest current densities[7].

Evidence exists to evaluate lower corrosion tendencies in spheroidized steels subjected to heat treatments, using H_2SO_4 as an electrolyte for the test[8]. However, when CO_2 is used, H_2CO_3 can be formed[9], an inorganic acid that helps to potentiate the corrosion process along with H_2SO_4, as shown in the reaction below.

$$CO_2 + H_2O \leftrightarrow H_2CO_3 \quad (1a)$$

$$2H_2CO_3 + 2e^- \rightarrow H_2 + 2HCO_3 \quad (1b)$$

$$2HCO_3 + 2e^- \rightarrow H_2 + 2CO_3^{2-} \quad (1c)$$

$$2H + + 2e^- \rightarrow H_2 \quad (1d)$$

$$Fe \rightarrow Fe_2^+ + 2e^- \quad (1e)$$

In reaction 1, an oxy-reduction is denoted, and in Equations 1b-1d, there are cathodic reactions (reduction) and

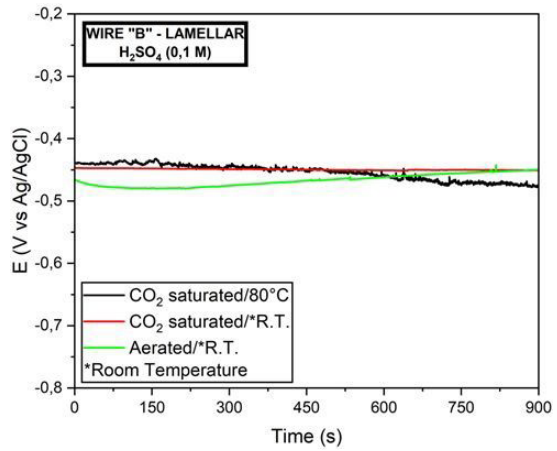

Figure 6. OCP curves for LC wire in aqueous solution of 0,1M H_2SO_4 with saturated CO_2 at 80 °C, saturated CO_2 at room temperature (23 °C) and aerated at room temperature (23 °C).

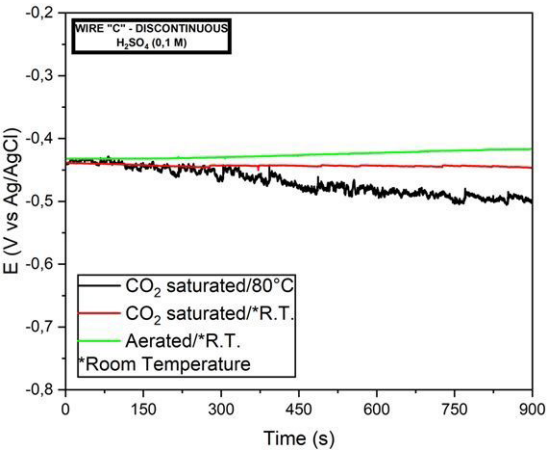

Figure 8. OCP curves for the DC wire in aqueous solution of 0,1M H_2SO_4 with saturated CO_2 at 80 °C, saturated CO_2 at room temperature (23 °C) and aerated at room temperature (23 °C).

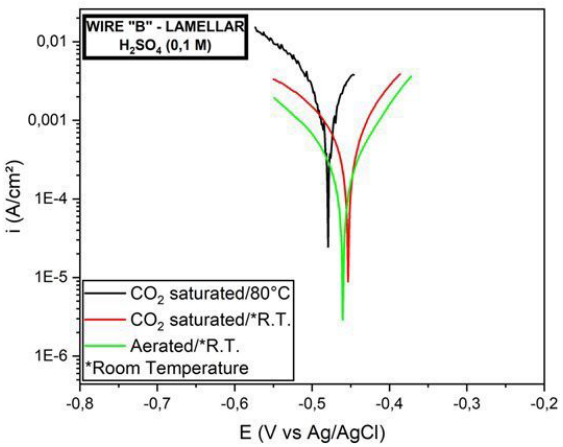

Figure 7. Potentiodynamic polarization curves for LC wire in aqueous solution of 3.5% NaCl with saturated CO_2 at 80 °C, saturated CO_2 at room temperature (23 °C) and aerated at room temperature (23 °C).

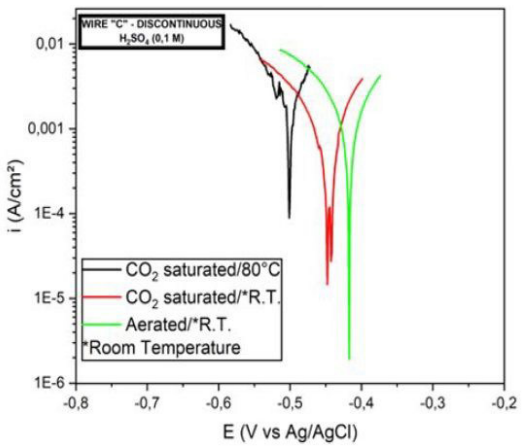

Figure 9. Potentiodynamic polarization curves for the DC wire in an aqueous solution of 0,1M H_2SO_4 with saturated CO_2 at 80 °C, saturated CO_2 at room temperature (23 °C) and aerated at room temperature (23 °C).

1e) anodic (oxidation). Evidence of this corrosion increase can be identified by comparing the pH of the tested solution. The sulfuric acid solution with saturated CO_2 presented a pH between 1-2 when used at a temperature of 80 °C, while when no CO_2 was used, pH values between 2 and 3 were reached.

3.2.2. Lamellar cementite wire

Figures 6 and 7 denote, respectively, graphs of open-circuit potential and linear potentiodynamic polarization. As in the curves for the PCE wire, no notable difference was identified between the potentials of these wires, leaving the current density data in Figure 7 as a way to differentiate them. The aerated solution at room temperature was the one with the lowest current density, so it was the least corroded. The aerated solution at room temperature continued to be the one in which there was less susceptibility to corrosion, denoting the medium as being less aggressive for the materials evaluated.

3.2.3. Brittle cementite wire

For discontinuous wire, the differences between the potentials were most remarkable (Figures 8 and 9). This information becomes more apparent when we compare the result of these potentials in solutions of CO_2 saturated at 80 °C and aerated at room temperature. This difference becomes even greater for potentiodynamic polarization since the less acidic solution (pH between 3-4) reaches current density values almost of the order of 1E-6.

3.3. Corrosion product characterization by Raman spectroscopy

Several characterization techniques can be applied to obtain information about the surface of a material, especially when it is subjected to corrosion. Among them, EDS (Electron Dispersive Spectroscopy) stands out[10], XRD (X-ray Diffraction)[11] and Raman Spectroscopy[5,12].

The main objective of this technique was to characterize salts and oxides located on the surface of the material after the corrosive process, especially $FeSO_4$ (ferrous sulfate) and $FeCO_3$ (siderite), which, according to the literature[13,14], to reduce the corrosive process.

3.3.1. LC sample in aqueous H_2SO_4 medium

The LC sample, as the one that obtained the best results in terms of corrosion resistance, was the wire submitted to the Raman spectroscopy characterization technique. Figure 10a indicates a region of the sample where distinct forms of corrosion are observed and which help to differentiate possible formation of oxides according to the morphology presented[15,16].

The square symbology inscribed in red in Figure 10a denotes a region of generalized corrosion where it is possible to obtain data on oxides or salts superimposed on layers in this sample[17]. Figure 10b indicates the Raman peaks in (cm-1) of the salts and oxides. Siderite ($FeCO_3$) and hydrated iron (II) sulfate ($FeSO_4$. $7H_2O$) reported in the literature as minimizing corrosion levels stand out[13].

Figure 10a, in the region identified by a red circle, characterizes an area without apparent corrosion or at least where there was no considerable formation of corrosion products. However, in Figure 10c, Raman oxides and a salt, namely $FeCO_3$, are revealed using the peaks. An interesting particularity is that in this region, there was no formation of S-based salt, which leads us to believe that these salts would be the main oxidant layers.

Also, in Figure 10a, a second symbology of the triangular type is observed, in which localized corrosion is observed[18]. Notably, it is a darker region amidst the region of widespread corrosion. In this region, ferrous sulfate was formed, and siderite was also found[19], and oxides relevant to the oxidation process, indicated in the wavelength peaks in Figure 10c.

4. Discussion

In this topic, the approach will compare the information identified in the results and point out solutions for the evaluations. Table 3 shows the information obtained in Figures 4-9 curves, considering the value of its corrosion potential and current density. For this last data, Tafel extrapolation was used[20-22]. This information is graphically represented in Figure 11 as a way to facilitate comparisons. Polarization resistance was calculated by the ratio between the electrochemical potential of the material and its current density, in what is called polarization resistance (PR).

The table also has statistical information such as the mean and deviation of the standard of the tests to identify the dispersion between each of the tests and their level of reproducibility.

From Table 3, it is possible to compare the three samples with their various solutions in OCP, current density, and, finally, their polarization resistance. For example, in the solution with saturated CO_2 at 80 °C, the highest resistance obtained was from the LC sample, although there was remarkable similarity between the calculated PRs. However, the lowest strength obtained was for SC wire. In solution 2, in line with the result of solution 1, the LC still had the highest PR value, but this time, with a very considerable

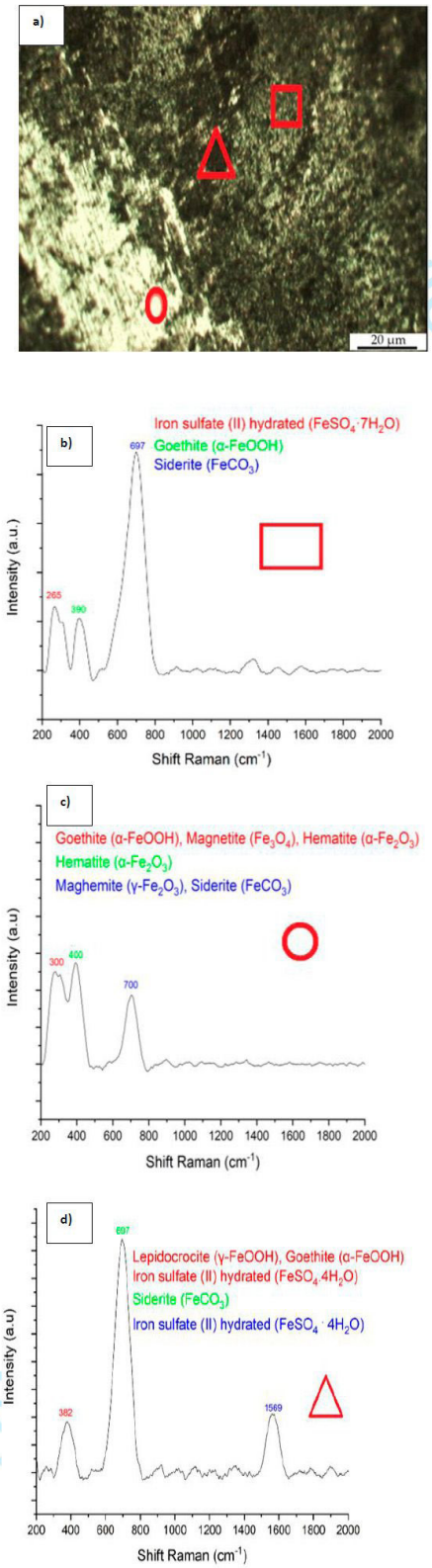

Figure 10. a) Scanned region of the LC sample with 3 distinct corrosion morphologies: generalized (□), no apparent corrosion (O) and localized (Δ); Raman peaks and their respective oxides for each type of corrosion: b) generalized; c) no apparent corrosion e d) localizaded.

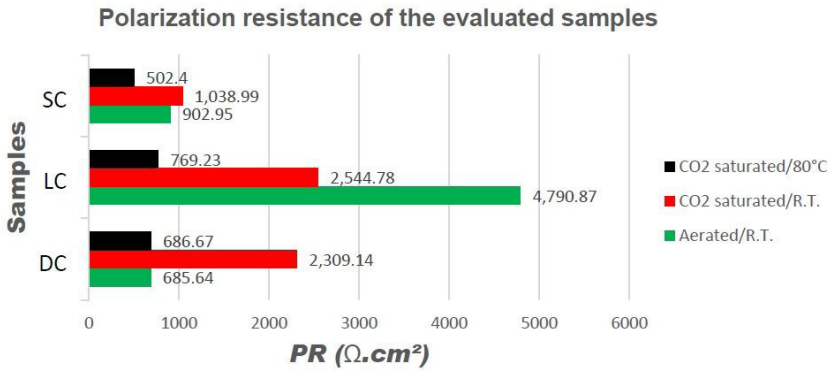

Figure 11. PR values calculated from the ratio between OCP and current density of the samples tested under each of the evaluated conditions.

Table 3. Statistical data from the electrochemical tests in H_2SO_4 for the three samples in the 3 tested solutions (MD = mean and SD = Standard Deviation).

WIRES	STATISTICS	Solutions (0,1 M H_2S0_4)								
		(1) Saturated CO_2/80 °C			(2) Saturated CO_2/R.T.			(3) Aerated/R.T.		
		Eletrochemical parameters								
		OCP (V vs Ag/AgCl)	I (A/cm²)	PR (Ω.cm²)	OCP (V vs Ag/AgCl)	I (A/cm²)	PR (Ω.cm²)	OCP (V vs Ag/AgCl)	I (A/cm²)	PR (Ω.cm²)
SC	MD	-0.50	9.89E-04	502.40	-0.42	4.21E-04	1,038.99	-0.41	4.72E-04	902.95
	SD	0.04	3.15E-05		0.00	8.40E-05		0.00	9.20E-05	
LC	MD	-0.47	6.33E-04	769.23	-0.45	1.79E-04	2,544.78	-0.44	9.19E-05	4,790.87
	SD	0.00	1.18E-04		0.01	2.45E-05		0.01	0.00	
DC	MD	-0.51	8.00E-04	686.67	-0.43	1.88E-04	2,309.14	-0.41	6.37E-04	685.84
	SD	0.02	2.00E-04		0.01	1.35E-05		0.00	1.58E-04	

jump in PR about the other samples, keeping the SC wire as the one with the lowest resistance to polarization. Finally, in the solution aerated at room temperature, the DC wire was the one with the lowest resistance, presenting less than 1/4 of the PR value of the LC wire.

The results of Table 3 state that the PCL were obtained the highest results for the three solutions evaluated. In contrast, the PCE wire presented low PR in 2 of the solutions, raising the question about the contribution of the different morphologies in a corrosive process. In addition to these, as stated by Ferhat et al.[23].

Other arguments evaluated and already addressed by other authors deal with the low corrosivity of lamellar microstructures. The lamellar structure corrodes at a relatively low rate because lamellar cementite forms preferential sites with less overpotential, favoring hydrogen evolution[24]. This leads to microgalvanic cells between the ferrite and cementite phases, providing a selective dissolution of the ferrite and influencing the kinetics of the reaction by the galvanic effect. This fact is not repeated in spheroidized structures because they have a high density and can more easily form galvanic pairs due to their reduced dimensions[25].

Ways to reduce this corrosion can be approached or at least minimized, such as forming passive films using adhesion when subjected to sulfuric media[24]. Carbon steels can form a protective layer of $FeSO_4$ on their metal surface when tested in sulfuric acid[26,27]. This reaction can be briefly summarized as indicated below:

$$H_2SO_4 + Fe \rightarrow FeSO_4 + H_2 \quad (2a)$$

This reaction can be further explained by electron exchange and divided into metal oxidation (anodic reaction) and hydrogen reduction (cathodic reaction)[28].

Anodic reaction: $Fe \rightarrow Fe_2 + + 2e-$ (2b)

Cathodic reaction: $2H + + 2e- \rightarrow H_2 \uparrow$ (2c)

The mechanism of anodic dissolution of iron helps to explain the presence of SO_4^{2-} anions in aqueous solutions[29], shown in the reaction 3a-3d down.

$$\left(H_2O\right)_{ads} + SO_4{}^{2-} \leftrightarrow H_2O + \left(SO_4{}^{2-}\right)_{ads} \quad (3a)$$

$$Fe + SO_4^{2-} \leftrightarrow \left(FeSO_4^{2-}\right)_{ads} \quad (3b)$$

$$\left(FeSO_4^{2-}\right)_{ads} \leftrightarrow \left(FeSO_4^{2-}\right) + 2e- \quad (3c)$$

$$\left(FeSO_4^{2-}\right)_{ads} \leftrightarrow Fe_2 + + SO_4^{2-} \quad (3d)$$

The above reactions indicate the formation of $(FeSO_4^{2-})$ ads when Fe is in contact with SO_4^{2-} ions, helping to explain the deposition of this salt in the assay samples.

The other Raman peaks evaluated in this sample and identified in Figures 10b-d are indicated below generalized corrosion region (265[30]; 390[31-35]; 697[36]); region without apparent corrosion (300[37,38]; 400[37,38]; 700[36]); region of localized corrosion (382[30,39]; 667[36]; 1569[36]). The spectra obtained here were individualized by the three regions distinguished in the sample regarding the degree of corrosion, and their peaks were surveyed according to the literature.

5. Conclusions

Based on the information obtained in the results and discussions, some conclusions can be indicated based on the electrochemical tests and characterization techniques ap-plied to the wires.

Under temperature conditions at 80 °C and with the use of CO_2, the lamellar micro-structure wire obtained higher PR results and, therefore, lower corrosion indexes, which can be admitted that for this result, there was a direct influence of siderite and ferrous sulfate as protective layers.

The influence of the formation of a $FeSO_4$ layer seems to be directly influenced by the siderite, since where the latter formed, the peak of $FeSO_4$ was greatly reduced compared to $FeCO_3$.

The Raman peaks, in addition to identifying the 2 salts addressed in the literature ($FeCO_3$ and siderite), also found several important oxides such as lepidocrocite, hematite and goethite.

The spheroidized microstructure in sulfuric medium showed lower results of PR and, therefore corrosion resistance, leading to the fact that its use should be limited in a sulfurous environment.

In a region of localized corrosion, siderite and ferrous sulfate salts were also found, which raises the question about the reduction of corrosion with these salts, which does not seem to have occurred in this area.

6. Acknowledgments

This study was supported by the Research and Support Coordenação de Aperfeiçoamento de Pessoal de Nível Superior Brasil (CAPES), Brazilian National Council for Scientific and Technological Development (CNPq).

The authors acknowledge with gratitude the team of the Materials Characterization Laboratory (LACAM), Analytical Central from Federal University of Ceará (UFC), Corrosion Research Laboratory (LPC), Coordenação de Aperfeiçoamento de Pessoal de Nível Superior Brasil (CAPES), and Brazilian National Council for Scientific and Technological Development (CNPq).

7. References

1. Amaechi CV, Reda A, Shahin MA, Sultan IA, Beddu SB, Ja'e IA. State-of-the-art review of composite marine risers for floating and fixed platforms in deep seas. Appl Ocean Res. 2023;138:103624. http://doi.org/10.1016/j.apor.2023.103624.
2. Li X, Jiang X, Hopman H. A review on predicting critical collapse pressure of flexible risers for ultra-deep oil and gas production. Appl Ocean Res. 2018;80:1-10. http://doi.org/10.1016/j.apor.2018.08.013.
3. Barros EV, Dias HP, Gomes AO, Rodrigues RRT, Moura RR, Sad CMS, et al. Study of degradation of acid crude oil by high resolution analytical techniques. J Petrol Sci Eng. 2017;154:194-203. http://doi.org/10.1016/j.petrol.2017.04.032.
4. Meriem-Benziane M, Bou-Saïd B, Boudouani N. The effect of crude oil in the pipeline corrosion by the naphthenic acid and the sulfur: a numerical approach. J Petrol Sci Eng. 2017;158:672-9. http://doi.org/10.1016/j.petrol.2017.08.073.
5. Choi Y-S, Colahan M, Nešić S. Effect of flow on the corrosion behavior of pipeline steel in supercritical CO_2 environments with impurities. Corrosion. 2023;79(5):497-508. http://doi.org/10.5006/4199.
6. Yang L, Liu Z, Yang X, Xu X, Cheng X, Li X. Behavior and evaluation of stress corrosion cracking of typical anchor bolt steel in simulated crevice environment. J Mater Res Technol. 2023;25:7430-43. http://doi.org/10.1016/j.jmrt.2023.07.149.
7. Abubakar SA, Mori S, Sumner J. Effect of dissolved CO_2 on the interaction of stress and corrosion for pipeline carbon steels in simulated marine environments. Metals. 2023;13(7):1165. http://doi.org/10.3390/met13071165.
8. Sarvghad M, Del Aguila D, Will G. Optimized corrosion performance of a carbon steel in dilute sulfuric acid through heat treatment. Appl Surf Sci. 2019;491:460-8. http://doi.org/10.1016/j.apsusc.2019.06.180.
9. Silva PN, Senatore EV, Gomes JACP. Corrosion of tensile wires covered with PA11 layers in simulated annulus environments at low CO_2 pressure. Mater Corros. 2023;74(2):306-19. http://doi.org/10.1002/maco.202213468.
10. Khan W, Tufail M, Chandio AD. Characterization of microstructure, phase composition, and mechanical behavior of ballistic steels. Materials. 2022;15(6):2204. http://doi.org/10.3390/ma15062204.
11. Elmourabit M, Allaoui I, Chaouket F, Draoui K, Ait Aghzzaf A, Raissouni I, et al. Valorization of phosphate sludge: synthesis of anti-corrosion pigments, physicochemical study and application to the protection of mild steel in a 3% NaCl medium. Waste Biomass Valoriz. 2023;14(12):4045-60. http://doi.org/10.1007/s12649-023-02034-6.
12. Sheikh AR. Effect of microalloying with Ti on the corrosion behaviour of low carbon steel in a 3.5 Wt.% NaCl solution saturated with CO_2. Arch Foundry Eng. 2022;23:5-10. http://doi.org/10.24425/afe.2023.144273.
13. Duboscq J, Abdelmoula M, Rémazeilles C, Jeannin M, Sabot R, Refait P. On the formation and transformation of fe(III)-containing Chukanovite, $Fe^{II}_{2-X}Fe^{III}_{x}(OH)_{2-X}O_xCO_3$. J Phys Chem Solids. 2020;138:109310. http://doi.org/10.1016/j.jpcs.2019.109310.
14. Li H, Chai F, Yang C, Li C, Luo X. Corrosion behavior of low alloy steel for cargo oil tank under upper deck conditions. J Iron Steel Res Int. 2018;25(1):120-30. http://doi.org/10.1007/s42243-017-0004-0.
15. Abdo HS, Seikh AH. Role of Nacl, CO_2, and H_2S on electrochemical behavior of 304 austenitic stainless steel in simulated oil industry environment. Metals. 2021;11(9):1347. http://doi.org/10.3390/met11091347.
16. Kratzig A, Hoa LQ, Bettge D, Menneken M, Bäßler R. Early stage of corrosion formation on pipeline steel X70 under oxyfuel

atmosphere at low temperature. Processes. 2020;8(4):421. http://doi.org/10.3390/pr8040421.
17. Shu Y, Yan M, Wei Y, Liu F, Han EH, Ke W. Characteristics of SRB biofilm and microbial corrosion of X80 pipeline steel. Acta Metall Sin. 2018;54:14081416. http://doi.org/10.11900/0412.1961.2018.00069.
18. Pessu FO, Saleem E, Espejo C, Neville A. Understanding the local pitting corrosion characteristics of carbon steel in CO_2 corrosion environment using artificially machined pits. Results Eng. 2022;16:100700. http://doi.org/10.1016/j.rineng.2022.100700.
19. Gong Q, Xiang Y, Zhang J, Wang R, Qin D. Influence of elemental sulfur on the corrosion mechanism of X80 steel in supercritical CO_2-saturated aqueous phase environment. J Supercrit Fluids. 2021;176:105320. http://doi.org/10.1016/j.supflu.2021.105320.
20. Azam MA, Safie NE, Hamdan HH. Effect of sulfur content in the crude oil to the corrosion behaviour of internal surface of API 5L X65 petroleum pipeline steel. Manuf Technol. 2021;21(5):561-74. http://doi.org/10.21062/mft.2021.066.
21. Pyshmintsev IY, Vavilova OV, Mansurova ER, Korober SA, Maltseva AN. Electrochemical investigation of the corrosion resistance of metal for oil and gas pipelines. Metallurgist. 2023;67(1-2):137-47. http://doi.org/10.1007/s11015-023-01497-1.
22. Yazıcı A, Zeybek MS, Kahraman F. Effect of different corrosive media on the corrosion resistance and mechanical properties of armor steel. Materialprüfung. 2023;65(7):1025-38. http://doi.org/10.1515/mt-2022-0362.
23. Ferhat M, Ferhat M, Benchettara A, Amara SE, Najjar D. Corrosion behaviour of fe-c alloys in a sulfuric medium. J Mater Environ Sci. 2014;5:1059-68.
24. López DA, Simison SN, de Sánchez SR. The influence of steel microstructure on CO_2 corrosion: EIS studies on the inhibition efficiency of benzimidazole. Electrochim Acta. 2003;48(7):845-54. http://doi.org/10.1016/S0013-4686(02)00776-4.
25. López DA, Schreiner WH, De Sánchez SR, Simison SN. The influence of carbon steel microstructure on corrosion layers: an XPS and SEM characterization. Appl Surf Sci. 2003;207(1-4):69-85. http://doi.org/10.1016/S0169-4332(02)01218-7.
26. Panossian Z, Silva CS, Santos M, Rufino CH, Pimenta GS, Silva CAM, et al. Corrosão do aço-carbono em ácido sulfúrico concentrado. In INTERCORR 2012; 2012; Salvador, BA. Anais. Rio de Janeiro: ABRACO; 2012.
27. Panossian Z, Almeida NL, Sousa RMF, Pimenta GS, Marques LBS. Corrosion of carbon steel pipes and tanks by concentrated sulfuric acid: a review. Corros Sci. 2012;58:1-11. http://doi.org/10.1016/j.corsci.2012.01.025.
28. Al-Moubaraki AH, Ganash AA, Al-Malwi SD. Investigation of the corrosion behavior of mild steel/H_2SO_4 systems. Mor J Chem. 2020;8(1):264-79.
29. Zhou Y, Guo L, Zhang S, Kaya S, Luo X, Xiang B. Corrosion control of mild steel in 0.1 M H_2SO_4 solution by benzimidazole and its derivatives: an experimental and theoretical study. RSC Adv. 2017;7(39):23961-9. http://doi.org/10.1039/C7RA02192E.
30. Chio HC, Sharma SK, Muenow DW. The hydrates and deuterates of ferrous sulfate ($FeSO_4$): a raman spectroscopic study. J Raman Spectrosc. 2007;38(1):87-99. http://doi.org/10.1002/jrs.1623.
31. Oh SJ, Cook DC, Townsend HE. Characterization of iron oxides commonly formed as corrosion products on steel. Hyperfine Interact. 1998;112(1-4):59-66. http://doi.org/10.1023/A:1011076308501.
32. Neff D, Dillmann P, Descostes M, Beranger G. Corrosion of iron archaeological artefacts in soil: estimation of the average corrosion rates involving analytical techniques and thermodynamic calculations. Corros Sci. 2006;48(10):2947-70. http://doi.org/10.1016/j.corsci.2005.11.013.
33. Ohtsuka T. Raman spectra of passive films of iron in neutral borate solution. Mater Trans JIM. 1996;37:67-9. http://doi.org/10.2320/matertrans1989.37.67.
34. Neff D, Bellot-Gurlet L, Dillmann P, Reguer S, Legrand L. Raman imaging of ancient rust scales on archaeological iron artefacts for long-term atmospheric corrosion mechanisms study. J Raman Spectrosc. 2006;37(10):1228-37. http://doi.org/10.1002/jrs.1581.
35. Neff DD, Reguer S, Bellot-Gurlet L, Dillmann P, Bertholon R. Structural characterisation of corrosion products on archaeological iron: an integrated analytical approach to establish corrosion forms. J Raman Spectrosc. 2004;35(8-9):739-45. http://doi.org/10.1002/jrs.1130.
36. Müller J, Speziale S, Efthimiopoulos I, Jahn S, Koch-Müller M. Raman spectroscopy of siderite at high pressure: evidence for a sharp spin transition. Am Mineral. 2016;101(12):2638-44. http://doi.org/10.2138/am-2016-5708.
37. Demoulin A, Trigance C, Neff D, Foy E, Dillmann P, L'Hostis V. The evolution of the corrosion of iron in hydraulic binders analysed from 46- and 260-year-old buildings. Corros Sci. 2010;52(10):3168-79. http://doi.org/10.1016/j.corsci.2010.05.019.
38. Dubois F, Mendibide C, Pagnier T, Perrard F, Duret C. Raman mapping of corrosion products formed onto spring steels during salt spray experiments: a correlation between the scale composition and the corrosion resistance. Corros Sci. 2008;50(12):3401-9. http://doi.org/10.1016/j.corsci.2008.09.027.
39. Li S, Hihara LH. A micro-raman spectroscopic study of marine atmospheric corrosion of carbon steel: the effect of Akaganeite. J Electrochem Soc. 2015;162(9):C495-502. http://doi.org/10.1149/2.0881509jes.